

IET Radar, Sonar & Navigation

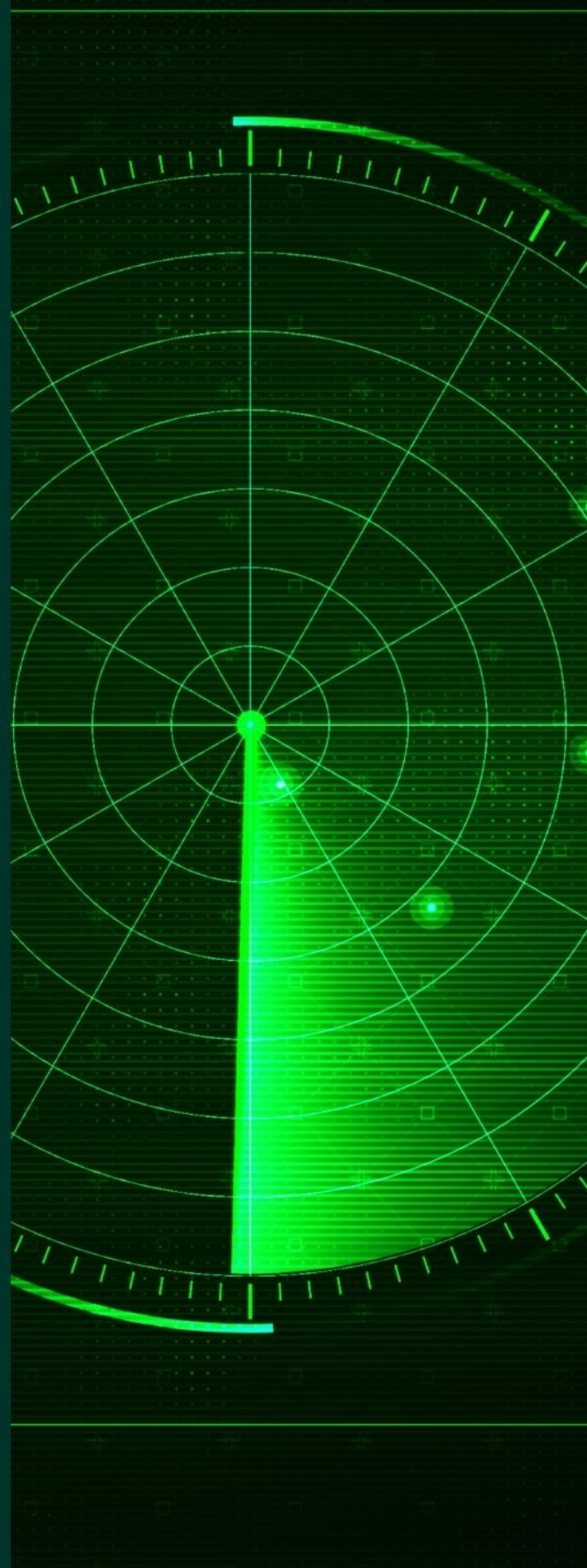
Special Issue Call for Papers

**Be Seen. Be Cited.
Submit your work to a new
IET special issue**

Connect with researchers and
experts in your field and
share knowledge.

Be part of the latest research
trends, faster.

[Read more](#)



The Institution of
Engineering and Technology

Three-dimensional Doppler-associated radar imaging method based on bi-directional data processing

Takumi Hayashi | Takeru Ando | Shouhei Kidera 

Graduate School of Informatics and Engineering,
The University of Electro-Communications, Tokyo,
Japan

Correspondence

Shouhei Kidera, Graduate School of Informatics
and Engineering, The University of Electro-
Communications, Tokyo, 1828585, Japan.
Email: kidera@uuc.ac.jp

Funding information

Japan Science and Technology Agency, Grant/
Award Number: JPMJPR1771; Precursory Research
for Embryonic Science and Technology

Abstract

Using a microwave or millimetre wave radar system, this study aims to achieve highly accurate Doppler velocity estimation and radar imaging that would be suitable for various remote-sensing sensors, such as self-driving, surveillance, or security applications. In particular, micro-Doppler signatures are one of the most promising approaches for human recognition; however, the traditional limitations of both velocity and temporal resolution need to be addressed. The weighted kernel density (WKD) algorithm using super-resolution Doppler velocity estimation has been one solution. Using WKD, this study incorporates the range points migration (RPM) method of radar imaging to enhance accuracy in both Doppler velocity and radar imaging using an iterative data selection scheme. Furthermore, to obtain more informative Doppler-associated RPM-based images using less data by exploiting a unique feature of WKD and RPM methods, this study introduces the image integration approach along the slow-time profile. In this framework, bi-directional data processing between Doppler velocity and imaging analysis is achieved. At each pulse hit sequence, both numerical and experimental tests demonstrate that the proposed method yields a more accurate Doppler-associated radar image compared with the methods in previous studies.

KEYWORDS

Doppler radar, millimetre wave radar, radar imaging, radar signal processing

1 | INTRODUCTION

Microwave or millimetre wave radar has a significant advantage such as non-line-of-sight imaging [1, 2] or human body recognition applications in the through-the-wall situation [3–6]. Many studies ([7–17]) have focussed on micro-Doppler analysis because of the micro-Doppler signatures developed using the various motions of the human body (such as arms, legs, torso and head). Traditional Doppler velocity analysis is based on the Fourier transform, such as the short-time Fourier transform (STFT) [17] and other derivative methods, such as the Radon-Fourier transform [18–21], the Fourier-Bessel transform [22], the keystone transform [23–25], the Hough transform [26–28], or the discrete polynomial phase transform [29], have been developed. However, because of the coherent integration process,

these methods have an inherent problem, that is there is a trade-off between temporal and velocity resolutions. Furthermore, at lower pulse repetition frequencies, the reflection echoes slide to another range gate at a different pulse hit, which is known as the range walk (RW) effect. For range resolution, certain super-resolution time-of-flight (TOF) estimations, such as multiple signal classification (commonly known as MUSIC), Capon, and compressed sensing (CS), have been proposed [30]. However, since these filters have very impulsive waveforms (narrower pulse width), they have considerably lower carrier frequencies, the RW problem could be more severe.

To overcome these limitations, an innovative Doppler velocity estimation algorithm, that is the weighted kernel density (WKD) estimator, has been developed [31]. The WKD method uses discrete TOF profiles (associated with the

This is an open access article under the terms of the Creative Commons Attribution License, which permits use, distribution and reproduction in any medium, provided the original work is properly cited.

© 2021 The Authors. *IET Radar, Sonar & Navigation* published by John Wiley & Sons Ltd on behalf of The Institution of Engineering and Technology.

slow time defined as τ), which are referred to as range- τ points (RPs), and converts this data to a corresponding estimated Doppler velocity using the Gaussian kernel-based probabilistic density function. A notable benefit of the WKD algorithm is that it provides us with an accurate Doppler velocity with no limit in resolution. This is because it evaluates the velocity using the inclination of the neighbouring range- τ points rather than phase rotation along the slow time. With a Doppler velocity value available at every pulse, temporal resolution is equivalent to the pulse repetition interval (PRI), which is derived from incoherent processing. A previous study [31] has reported that, when used in combination with super-resolution range techniques, that is a CS filter, the WKD method offers a distinct improvement in performance because it does not require phase responses and maintains its performance even with lower carrier frequency signals. However, for cases in which a target has multiple reflection points, similar to a human body, the WKD method still suffers from inaccuracy because of interference in the reflection signals.

To address this interference-related issue in the former method [31], this study newly introduces a bi-directional data processing scheme to process data between an accurate radar imaging method known as the range point migration (RPM) method [32] and the WKD Doppler velocity algorithm. Various radar imaging approaches are available, including synthetic aperture radar [33], Kirchhoff migration [34, 35], range migration algorithm [36, 37], and holographic imaging [38–40]. These methods are based on coherent integration and should satisfy the Nyquist criterion for sampling interval of observation points to avoid an ambiguous response due to phase uncertainty. On the other hand, RPM uses incoherent data conversion from the observed range- τ points (associated with the sensor location) to the corresponding reflection point (dominant scattering centre) of the target boundary. Given that image reconstruction from RPM is based on the point-cloud rather than the spatial profile of strength used in conventional radar imaging, resolution is not limited by the wavelength or aperture size, but rather by the accuracy of range point extraction: that is the signal-to-noise ratio (SNR) and signal bandwidth. In addition, a previous study [41] looked at Doppler velocity-associated RPM imaging of the human body focussing on a unique feature of RPM: Each range- τ point can be associated with a particular Doppler velocity and reflection point, with a one-to-one correspondence. Also, bi-directional data processing can be implemented for Doppler velocity-associated radar imaging, the basic idea of which has been introduced in Ref. [42]. For this application, data flowing from RPM to WKD would mean that each range- τ was weighted by a prior RPM image (space prior) in the WKD algorithm; therefore, the range- τ points from the same part of the human body could be processed in the WKD algorithm, thus effectively eliminating range- τ points' interference. The other direction (WKD to RPM) compensates the points along a slow-time profile, which indicates that the number of processed range

points would increase and provide a more accurate and informative RPM image. This application is significant because an RPM image is determined by aggregating reconstructed reflection points. A smaller number of reconstruction points result in a less-informative image, which occurs when there are a limited number of arrays or observation samples. The WKD to RPM scheme would address this by increasing the number of range- τ points (that of the reflection points) with the neighbouring pulse hits. The three-dimensional (3-D) FDTD-based numerical tests, assuming a human target with walking motion, show that our proposed method, namely the bi-directional data processing scheme, considerably enhances accuracy in both Doppler velocity and image estimations. In addition, the experimental validations with three metallic spheres with X-band ultra-wideband (UWB) radar equipment demonstrate the effectiveness of the proposed method, in terms of Doppler velocity and reconstruction accuracy, which has not been demonstrated in Ref. [42].

2 | OBSERVATION MODEL

The observation and target model, applying a 2-D multiple-input-multiple-output (MIMO) radar, is illustrated in Figure 1. A number of pulses are transmitted from the transmitter with fixed PRI at each timing τ , which is the so-called 'slow time.' The planar array contains multiple transmitters and receivers, the locations of which are denoted as L_T and L_R , respectively. $s(L_T, L_R, R, \tau)$ is an output of the range extraction filter (e.g, matched, Wiener, or CS filters) observed at the combination of L_T and L_R at the slow time τ , which is given by an integer multiple of PRI. Here, $R = ct/2$ is determined by a fast time t and the speed of the radio wave is c . Note that the local maxima of $|s(L_T, L_R, R, \tau)|$ denote the number of discrete ranges from each element combination to the target reflection point, which are called as range- τ points. Then, to extract a

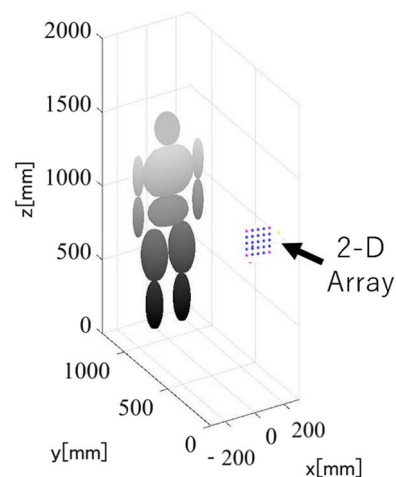


FIGURE 1 Observation model

reflection point on the target boundary or its associated Doppler velocity for each set of range and elements combination, the j -th range- τ point as $\mathbf{q}_{i,j} \equiv (\mathbf{L}_{i,j}^T, \mathbf{L}_{i,j}^R, R_{i,j}, \tau_i)$ at the slow time τ_i is defined. $\mathbf{q}_{i,j} \equiv (\mathbf{L}_{i,j}^T, \mathbf{L}_{i,j}^R, R_{i,j}, \tau_i)$ is extracted as follows:

$$\left. \begin{aligned} \frac{\partial s(\mathbf{L}_T, \mathbf{L}_R, R, \tau)}{\partial R} &= 0 \\ s(\mathbf{L}_T, \mathbf{L}_R, R, \tau) &\geq \alpha \max_{R, \tau} s(\mathbf{L}_T, \mathbf{L}_R, R, \tau) \end{aligned} \right\}, \quad (1)$$

where α denotes the threshold parameter. This relevance of this model has been demonstrated in the literature [31, 32].

3 | EXISTING METHODS

3.1 | Radar imaging method

Our primary goal is associating radar imaging with Doppler velocity for target recognition such as a human body, and then, we introduce the RPM method [32], at the first step of the proposed method, as follows. The RPM method uses a batch conversion scheme from a group of measured range- τ points (called as RP) and their corresponding scattering centres. In the RPM, each scattering centre point $\hat{\mathbf{p}}(\mathbf{q}_{i,j})$ associated with $\mathbf{q}_{i,j}$ at the slow time τ_i is determined as follows:

$$\begin{aligned} \hat{\mathbf{p}}(\mathbf{q}_{i,j}) &= \arg \max_{\mathbf{p}^{\text{int}}(\mathbf{q}_{i,j}; \mathbf{q}_{i,m}, \mathbf{q}_{i,n}) \in P_{i,j}(\mathbf{q}_{i,k}, \mathbf{q}_{i,l}) \in Q_{\text{all}}} \sum g(\mathbf{q}_{i,j}; \mathbf{q}_{i,k}, \mathbf{q}_{i,l}) \\ &\times \exp \left\{ - \frac{\| \mathbf{p}^{\text{int}}(\mathbf{q}_{i,j}; \mathbf{q}_{i,k}, \mathbf{q}_{i,l}) - \mathbf{p}^{\text{int}}(\mathbf{q}_{i,j}; \mathbf{q}_{i,m}, \mathbf{q}_{i,n}) \|}{2\sigma_r^2} \right\}. \end{aligned} \quad (2)$$

where $\mathbf{p}^{\text{int}}(\mathbf{q}_{i,j}; \mathbf{q}_{i,k}, \mathbf{q}_{i,l})$ or $\mathbf{p}^{\text{int}}(\mathbf{q}_{i,j}; \mathbf{q}_{i,m}, \mathbf{q}_{i,n})$ shows the intersection points between the three spheroids determined by $\mathbf{q}_{i,j}, \mathbf{q}_{i,k}$ and $\mathbf{q}_{i,l}$ or $\mathbf{q}_{i,j}, \mathbf{q}_{i,m}$ and $\mathbf{q}_{i,n}$, respectively. Each spheroid has focal points \mathbf{L}_T and \mathbf{L}_R and a major radius R and $P_{i,j}$ is a set of the intersection points between the three spheroids, which is determined by each $\mathbf{q}_{i,j}$. $g(\mathbf{q}_i; \mathbf{q}_j, \mathbf{q}_k)$ is defined as follows:

$$\begin{aligned} g(\mathbf{q}_i; \mathbf{q}_j, \mathbf{q}_k) &= s(\mathbf{q}_j) \exp \left\{ - \frac{D(\mathbf{q}_i, \mathbf{q}_j)}{2\sigma_D^2} \right\} \\ &+ s(\mathbf{q}_k) \exp \left\{ - \frac{D(\mathbf{q}_i, \mathbf{q}_k)}{2\sigma_D^2} \right\}, \end{aligned} \quad (3)$$

where σ_D denotes the parameter for the correlation length along a sensor location. $D(\mathbf{q}_i, \mathbf{q}_j)$ is defined as follows:

$$D(\mathbf{q}_i, \mathbf{q}_j) = \min \left(\| \mathbf{L}_{T,i} - \mathbf{L}_{T,j} \|^2 + \| \mathbf{L}_{R,i} - \mathbf{L}_{R,j} \|^2, \| \mathbf{L}_{T,i} - \mathbf{L}_{R,j} \|^2 + \| \mathbf{L}_{R,i} - \mathbf{L}_{T,j} \|^2 \right). \quad (4)$$

In this algorithm, each scattering centre is determined from all possible intersection points of the spheroids, determined by other RPs (known as SubRPs), where any connection or tracking procedure of the RPs could be avoided by the WKD estimation-based batch processing in Equation (2). The RPM method has a notable feature, that is it is not derived from other radar imaging methods: the scattering centre point $\hat{\mathbf{p}}(\mathbf{q}_{i,j})$ is reversibly associated with each range- τ point $\mathbf{q}_{i,j}$, which enables multi-functional imaging using Doppler velocity [41]. Note that, in the presence of multiple objects, a large number of SubRPs should be processed for each MainRP, which incurs an excessive increase of the computational cost and inaccuracy in the reconstruction. Reference [41] shows that using a RP clustering scheme prior to estimating Doppler velocity is effective in enhancing both computational speed and accuracy, where one RP generated by the right arm should be processed using SubRPs obtained from the same area of the arm, while irrelevant RPs should be eliminated in the RPM process. Therefore, to reduce the computational complexity and enhance the accuracy in this model, Doppler velocity-based RP clustering is required.

3.2 | Doppler velocity estimation method

3.2.1 | WKD algorithm

As an innovative Doppler velocity estimation method, the WKD method has been first introduced in Ref [31]. The WKD method incoherently converts a discrete range- τ point to its corresponding Doppler velocity- τ point, through an optimisation process using a weighted Gaussian kernel density estimator. This method overcomes the traditional limitation of balancing the temporal and velocity resolutions, which is inherent in a coherent integration-based Doppler analysis, such as STFT. Here, the methodology of the WKD is briefly described as follows. Focussing on one range- τ point as $\mathbf{q}_{i,j}$, its associated Doppler velocity $\hat{v}_d(\mathbf{q}_{i,j})$ can be determined by a radial difference from the neighbouring range- τ along the τ direction. Then, the optimal Doppler velocity is determined as follows:

$$\begin{aligned} \hat{v}_d(\mathbf{q}_{i,j}) &= \arg \max_{v_d} \sum_{k,l} \exp \left(- \frac{|s(\mathbf{q}_{i,j}) - s(\mathbf{q}_{k,l})|^2}{2\sigma_s^2} \right) \\ &\times \exp \left(- \frac{|\tau_i - \tau_k|^2}{2\sigma_\tau^2} \right) \exp \left(- \frac{|v_d - v_{d,i,j,k,l}|^2}{2\sigma_{v_d}^2} \right), \end{aligned} \quad (5)$$

where $v_{d,i,j,k,l} \equiv (R_{i,j} - R_{k,l}) / (\tau_i - \tau_k)$. The connecting or tracking processes for range- τ points is not necessary for calculating Equation (5), which considerably reduces the computational complexity. A number of advantages of this method have been verified in several studies [31]. The most distinguished advantage of the WKD is that it avoids any trade-off between temporal and velocity resolution. In

traditional coherent integration schemes such as STFT and Radon-Fourier transforms, Doppler velocity is determined from phase rotation of the carrier frequency, and there is a strict trade-off between temporal and velocity resolution. However, as we have already seen, WKD calculates an inclination between the neighbouring range- τ points as $v_{d,i,j,k,l}$ at each slow time, so it avoids phase ambiguities. Note that with WKD there is no lower limit for both Doppler velocity and temporal resolution, as detailed in [31]. However, when we deal with an object with many scattering centres, such as a human body, the object still suffers from lower accuracy. This is attributed to each Doppler velocity, $\hat{v}_d(q_{i,j})$ being determined using all possible range- τ points via Equation (5), which includes unnecessary range- τ points derived from different parts of the human body. Furthermore, a prior clustering or data selection scheme is required to obtain a sufficient level of accuracy and to achieve lower computational costs, which is similar to the previous RPM imaging scheme described in Section 3.1. However, the above prior knowledge is hardly available in the actual scenario.

4 | PROPOSED METHODS

4.1 | Bi-directional data processing with RPM and WKD

To address the difficulties mentioned in Sections 3.1 and 3.2.1, interactive processing between RPM and WKD is proposed

here. In our proposed scheme, the Doppler velocity by WKD and the 3-D radar image by RPM are recursively updated to upgrade their accuracies. Figure 2 shows the conceptual figure of the proposed scheme. First, the processing for RPM \rightarrow WKD is presented as follows. To enhance the accuracy of the Doppler velocity using the WKD estimator, a prior clustering of range- τ points is promising. Thus, an initial Doppler velocity is determined by the original WKD method as shown in Equation (5), which is denoted as $\hat{v}_d^{(1)}(q_{i,j})$. All range- τ points are then clustered into a subset $Q_T^{(1)}$ by collecting those that have similar Doppler velocities as $\hat{v}_d^{(1)}(q_{i,j})$.

Then, at the n -th iteration process, the scattering centre $\hat{p}^{(N)}(q_{i,j})$ is determined using the RPM scheme as follows:

$$\hat{p}^{(N)}(q_{i,j}) = \arg \max_{p^{\text{int}}(q_{i,k}; q_{i,m}; q_{i,n}) \in P_{ij}} \sum_{(q_{i,k}; q_{i,l}) \in Q_T^{(N)}} g(q_{i,j}; q_{i,k}, q_{i,l}) \times \exp \left\{ - \frac{\|p^{\text{int}}(q_{i,j}; q_{i,k}, q_{i,l}) - p^{\text{int}}(q_{i,j}; q_{i,m}, q_{i,n})\|}{2\sigma_r^2} \right\}, \quad (6)$$

where N denotes the iteration number of bi-directional data processing. The Doppler velocity is updated as follows:

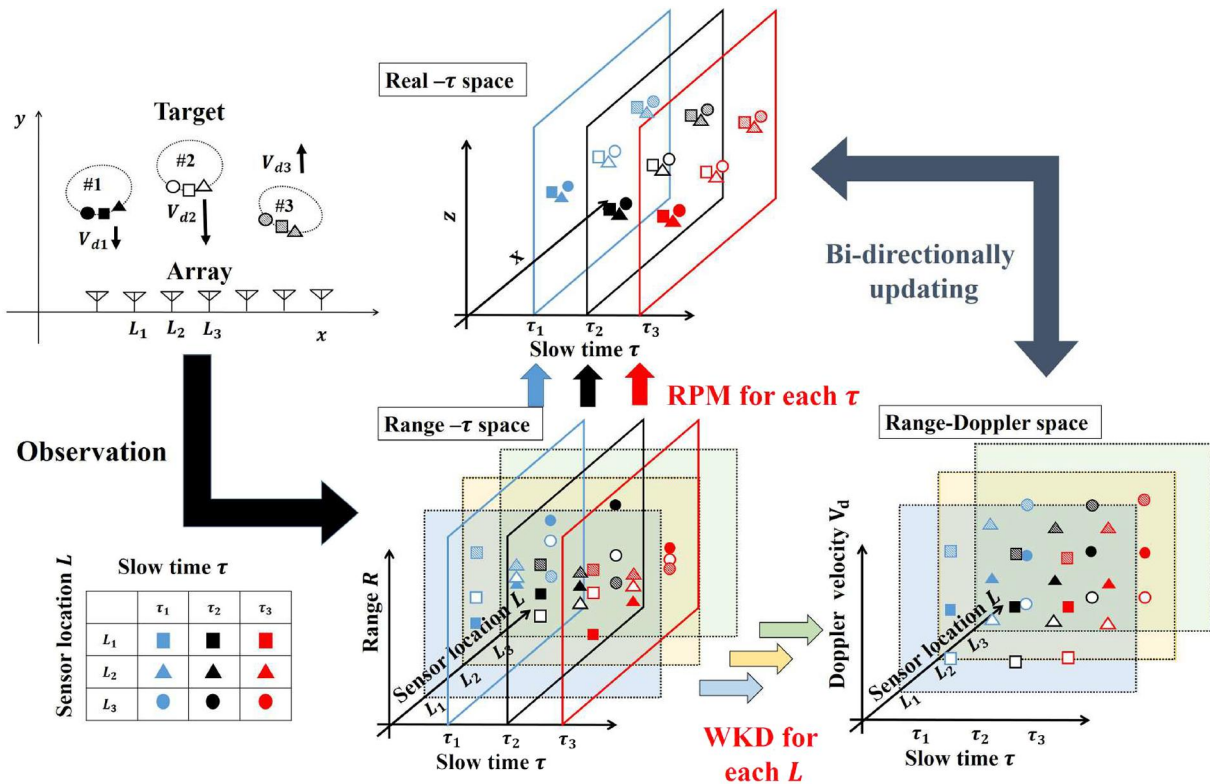


FIGURE 2 Data processing sequences in the proposed method

$$\begin{aligned}
 v_d^{(N)}(q_{i,j}) = \arg \max_{v_d} \sum_{k,l} \exp \left(- \frac{|s(q_{i,j}) - s(q_{k,l})|^2}{2\sigma_s^2} \right) \\
 \times \exp \left(- \frac{|\tau_i - \tau_k|^2}{2\sigma_\tau^2} \right) \exp \left(- \frac{|v_d - v_{d,i,j,k,l}|^2}{2\sigma_{v_d}^2} \right) \\
 \times \exp \left(- \frac{\|\hat{p}^{(N)}(q_{i,j}) - \hat{p}^{(N)}(q_{k,l})\|^2}{2\sigma_p^2} \right), \tag{7}
 \end{aligned}$$

The term $\exp \left(- \frac{\|\hat{p}^{(N)}(q_{i,j}) - \hat{p}^{(N)}(q_{k,l})\|^2}{2\sigma_p^2} \right)$ shows the data selection of the scattered centre points $\hat{p}^{(N)}(q_{i,j})$, where $q_{k,l}$ is eliminated if the distance between $\hat{p}^{(N)}(q_{i,j})$ and $\hat{p}^{(N)}(q_{k,l})$ is significantly larger, indicating that it is derived from different parts of the object. This data selection scheme is based on the fact that the one set of range- τ points is derived from a specific part of the human body and should be processed using the same cluster in the WKD process.

For an insufficient volume of data, for example with small array configuration, the RPM can hardly provide an informative image because of the small number of scattering centre points. Thus, the data (range- τ points) integration along the slow-time profile enables us to enhance the number of imaging points and the accuracy, which motivates the following image integration scheme. Figure 3 shows the schematic diagram of the data integration of the proposed method, described below. The actual procedure of the proposed method is detailed as follows:

- Step (1) A range extraction filter (e.g. matched, Capon or CS filters) is applied to the received signals at each slow time τ , denoted as $s(L_T, L_R, R, \tau)$.
- Step (2) Range- τ points $q_{i,j}$ are extracted from the local maxima of $s(L_T, L_R, R, \tau)$ as shown in Equation (1).
- Step (3) An initial estimate for the Doppler velocity is determined as $\hat{v}_d^{(1)}(q_{i,j})$ in Equation (5), and $N = 1$ is set.

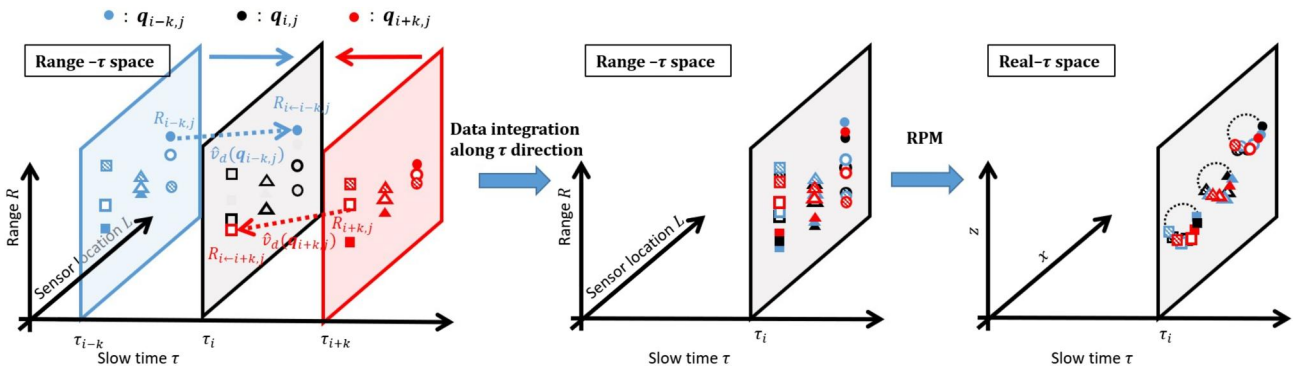


FIGURE 3 Schematic illustration for data integration along slow time direction

- Step (4) Range- τ points are clustered in terms of the Doppler velocity, and each set of clusters is denoted as $Q_I^{(N)}$.
- Step (5) For each subset of range- τ as $Q_I^{(N)}$, the RPM determines its associated scattering centre as $\hat{p}^{(N)}(q_{i,j})$ shown in Equation (6). The scattering centres with a significantly lower evaluation value, the right side of Equation (6), are eliminated, and their associated range- τ points are also deleted from the previous set.
- Step (6) The Doppler velocity for each range- τ point are updated as $\hat{v}_d^{(N+1)}(q_{i,j})$ in Equation (7), where the range- τ points with significantly lower evaluation values, and the right side of Equation (7), are eliminated.
- Step (7) $N \rightarrow N + 1$ and return to Step (4).
- Step (8) For image integration along the slow time direction, each member $R_{i\pm 1,j}$ of $q_{i\pm 1,j}$ in the neighbouring range- τ points is compensated as follows:

$$R_{i\leftarrow i-k,j} = R_{i-k,j} + \hat{v}_d^{(N+1)}(q_{i-k,j}) k\Delta\tau \tag{8}$$

then, the range- τ points are redefined as follows:

$$q_{i-k,j} \equiv (L_{i,j}^T, L_{i,j}^R, R_{i-k,j}, \tau_i) \tag{9}$$

- Step (9) Finally, for integrated range- τ points, using $q_{i,j}$ and $q_{i\leftarrow i-k,j}$, the RPM process is applied in Equation (6).

Figure 4 shows the flowchart of the proposed method, separated by the bi-directional processing and data integration steps.

5 | NUMERICAL VALIDATION

5.1 | Numerical setting

In this section, the 3-D FDTD-based numerical examples are validated, in which a simplified human target was introduced to assess the performance in both Doppler velocity estimation and the 3-D image integration scheme. A pulse modulated

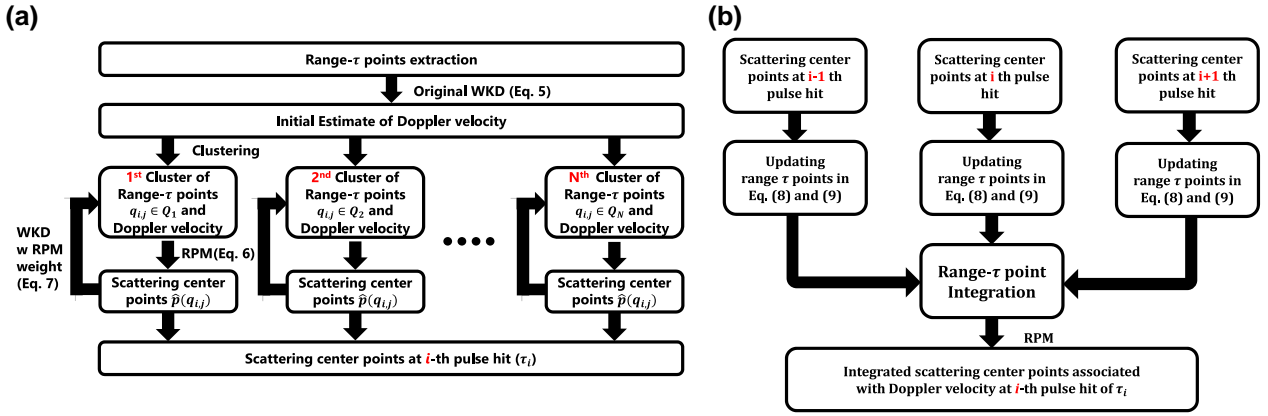


FIGURE 4 Flowchart of the proposed method. (a) Bi-directional processing Step (1) to Step (7). (b) Data integration step as Steps (8) and (9)

TABLE 1 Numerical setting of motion velocity along the y axis for each part of the human body

Doppler velocity	Parts
-1.0 m/s	Right lower arm & left lower leg
-0.5 m/s	Right upper arm & left upper leg
0 m/s	Head & lower and upper torso
0.5 m/s	Left upper arm & right upper leg
1.0 m/s	Left lower arm & right lower leg

signal with a centre frequency set at 5.0 GHz and 3 dB bandwidth set at 3.0 GHz was used as a transmitting current, that is, the theoretical range resolution is 50 mm, in this case. As shown in Figure 1, the human body is composed of 11 ellipsoids, each representing a part of the body. The ellipsoids had a relative permittivity of 50 and conductivity of 1.0 S/m, which corresponded to the average values for human tissues. This simplified human model was used to conduct a quantitative assessment of the range, Doppler velocity, and 3-D imaging estimations, something difficult to achieve in a more accurate model as in Ref. [43]. The planar array was configured in a 5×5 antennae square with 50 mm equal spacing along the $y = 0$ plane. A transmitter was placed at each corner of this square array, and the 5×5 antennae were used as receivers, which indicate that 100 combinations were processed in each slow time τ . Here, it is assumed that a human step should be at position $y = 1000$ mm, where each motion vector of the ellipsoid had only the y component. Table 1 shows each part's motion velocity along the y axis, and each velocity is invariant in all pulse sequences and that the assumption could be established in a short observation period. Here, we assumed the pulse sequenced with a 20.0 ms PRI and the total number of pulse hits was 10, making the duration for the pulse sequences $T_c = 0.2$ s, and it shows a 0.15 m/s theoretical Doppler velocity resolution assuming the centre frequency of 5.0 GHz and an unambiguous velocity range of ± 0.75 m/s, in assuming the Fourier transform-based analysis. Thus, the Doppler velocity of the lower arm or leg exceeds the upper limitation of the unambiguous velocity range in using the

STFT scheme. A noise-free environment is assumed to validate an inherent performance for each method.

5.2 | Results in Doppler velocity estimation

Figure 5 shows Doppler velocity estimations obtained by the method from [31] and those from the proposed method of two representative combinations at $\tau = \tau_5$. As shown in this figure, a number of actual range- τ points from multiple parts of human body exist within a range resolution cell (50 mm), and these points are hardly separated using the traditional filter, such as matched filter, which has also been demonstrated in Ref. [31]. It should be also noted that the literature [31] demonstrated that a simple Doppler-range separation scheme using the STFT and matched filtering could not separate the actual range-Doppler profile, due to RW problem and lower temporal and velocity resolutions, in the same model assumed in this simulation. Thus, in this study, the super-resolution CS filter [30] is applied for the range extraction filter, this is because a desired range profile is expressed as an aggregation of Dirac's Delta function, and such profile generally has a sparse feature. Furthermore, while the actual Doppler velocities of lower arms or legs exceed the unambiguous velocity range (± 0.75 m/s), the WKD-based method provided accurate Doppler velocity over the above range, i.e., a distinguished advantage of the WKD over the Fourier transform-based method. Table 2 also shows the quantitative error evaluations in which all pulse hits and sensor combinations are counted. ΔR and Δv_d denote the errors for range and Doppler velocity, respectively, and these comparisons show that the bi-directional data processing scheme remarkably enhanced the performance of Doppler velocity estimation using the RPM-based data selection scheme, and it enhanced the cumulative probability by eliminating unnecessary estimators of Doppler velocity via Steps (5) and (6) in the proposed method.

Furthermore, as described in Section 4.1, we investigated the range compensation scheme in the data integration along the slow-time profile direction, using Equation (8) at Step (8) in the proposed method. Figure 6 shows the range-Doppler

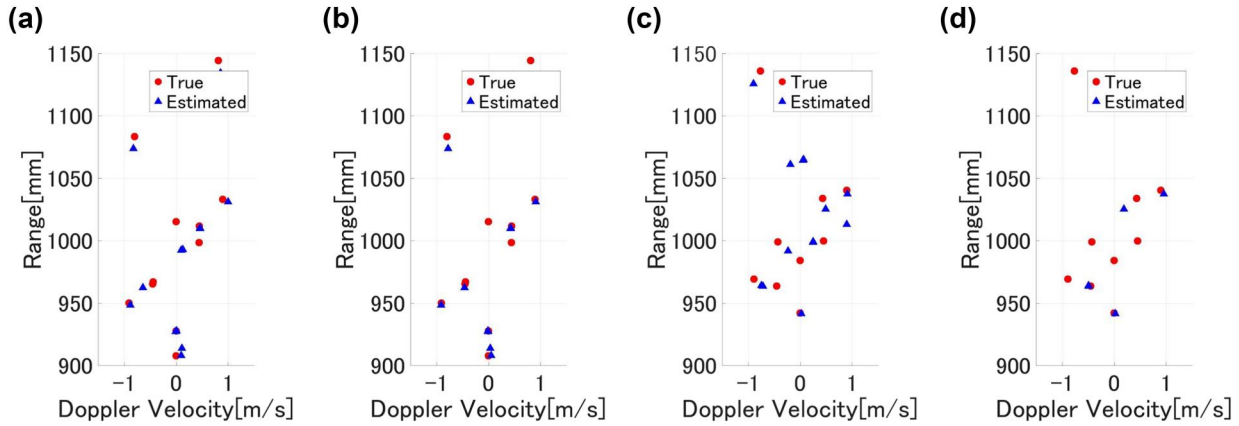


FIGURE 5 Range-Doppler velocity estimation results at $\tau = \tau_5$ on $L_T = (-100, 0, 900)$, $L_R = (50, 0, 1000)$. (a) Method [31], (b) proposed, (c) method [31] and, (d) proposed

TABLE 2 Cumulative probability of each criteria in the Doppler velocity estimation

	Method [31]	Proposed
$ \Delta R \leq 10$ mm and $ \Delta v_d \leq 0.1$ m/s	34.3 % (5946/17336)	77.1 % (7760/10065)
$ \Delta R \leq 20$ mm and $ \Delta v_d \leq 0.1$ m/s	42.7 % (7402/17336)	85.7 % (8625/10065)
$ \Delta R \leq 20$ mm and $ \Delta v_d \leq 0.2$ m/s	60.3 % (10453/17336)	94.8 % (9541/10065)

velocity profile at $\tau = \tau_5$, where each range–Doppler velocity point is updated along the range direction using each method. Note that, for the method in [31], $R_{i \pm 1, j}$ is simply updated by the initial Doppler velocity as determined in Equation (5). Table 3 summarises the quantitative error evaluations for ΔR and clarifies that our proposed method updated the range values more accurately compared to a previously reported method [31] because an accurate Doppler velocity profile correctly compensates the range R . Thus, these results confirm that our method is more suitable as a data integration scheme along the slow-time profile; the amount of processed

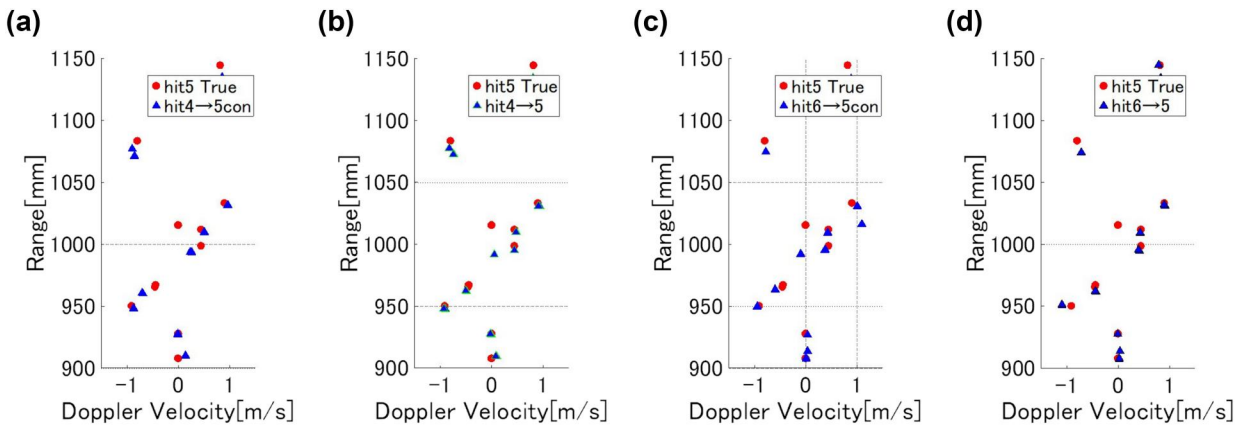


FIGURE 6 Range compensation results at τ_5 on $L_T = (-100, 0, 900)$, $L_R = (50, 0, 1000)$ (a) Method [31], (b) proposed, (c) method [31], and (d) proposed. (a and b) $\tau_4 \rightarrow \tau_5$. (c and d) $\tau_6 \rightarrow \tau_5$

TABLE 3 Cumulative probabilities for range points compensations at each criteria

	5		4 \rightarrow 5		6 \rightarrow 5	
	Method [31]	Proposed	Method [31]	Proposed	Method [31]	Proposed
$ \Delta R \leq 5$ mm	46.6%	73.3%	47.6%	57.1%	50.0%	55.5%
$ \Delta R \leq 10$ mm	53.3%	86.6%	57.1%	100%	70.0%	83.3%
$ \Delta R \leq 20$ mm	80.0%	100%	80.1%	100%	90.0%	100%

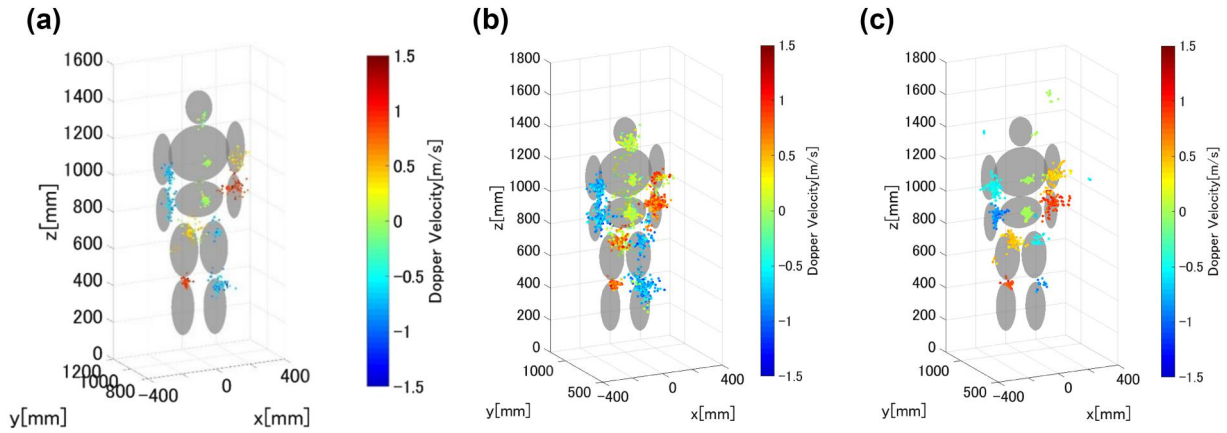


FIGURE 7 Range points migration image integration results by each method at τ_5 , where the range- τ data at τ_4 and τ_6 are integrated in (b and c). (a) Method [31] w/o integration (b) method [31] w integration, and (c) proposed method w integration

TABLE 4 Cumulative probability and RMSE for the range points migration imaging with or without data integration

	Cumulative probability for err ≤ 10 mm	RMSE
Method [31] w/o data integration	61% (465/757)	20.6 mm
Method [31] w data integration	51% (1285/2509)	31.5 mm
Proposed method [31] w data integration	76.5% (1550/2025)	30.3 mm

Abbreviation: RMSE, root mean square errors.

data (the number of range- τ points) is significantly increased, leading to a more accurate and informative image.

5.3 | Results in RPM image integration

For RPM imaging, the data integration scheme is sequentially illustrated in Figure 7, where the range- τ points at τ_5 are added from those obtained at τ_4 and τ_6 using the Doppler velocity for each method. Table 4 summarises the cumulative probabilities and root mean square errors for imaging performance, with or without data integration. These results confirm that, using the data integration in the RPM framework, the enhancement for Doppler velocity estimation leads to more accurate and informative imaging. Note that, the spread of scattering centre points is significantly reduced by the proposed method, compared with that obtained by Method [31], which has been indicated that the total number of RPM imaging points within 10 mm accuracy would increase more than that using Method [31]. Furthermore, while the Method [31] could not clearly separate the Doppler velocity between the lower and upper parts of arm and legs (different colour points are mixed in each arm and leg) as shown in Figure 7, the proposed method could clearly separate the Doppler velocity points on the correct part of human body (same colour points are allocated to each arm and leg) as in Figure 7c. This is because the proposed method integrates the range- τ points with more accurate Doppler velocity points, which is the definitive advantage from the previous method [31]. We should note that accuracy in range point

compensation for ‘6→5’ is slightly better than that of ‘4→5’ because at the moment of the later pulse (6) each part of human body may be more separated. In that case, we may obtain more accurate range- τ profiles with the same range resolution.

5.4 | Discussions for applicability

Here, we discuss the applicability of the proposed method, assuming other observations or the target model. In the numerical model described in Section 5, the maximum velocity of all body parts is no higher than 1.0 m/s in the simulation, for which the parameters are determined by our previous experiment. On the contrary, if we assume a faster walking motion, the maximum velocity may rise to 5 m/s. However, we could consider that if the motion velocity was higher than that assumed in this study, the range- τ profile could be extracted more accurately because each part of the human body, the arm or leg would have a separation larger than that of the range resolution. In addition, traditional STFT or coherent integration cannot cover such a larger velocity range, given the phase uncertainty involved. That is certainly the case with a model in which the unambiguous velocity range is limited to ± 0.75 m/s with a 20 ms PRI. But with each range- τ point converted to its associated Doppler velocity via an incoherent process in the WKD method, there is no such limitation for the maximum velocity, and that is the advantage of the WKD. For this reason the WKD is a far better way to deal with faster moving objects.

Note that the realistic motion of each body part is time variant, whereas the numerical model described in Section 5 assumes time-invariant motion in each part. This is because in a period with 10 transmitted pulses and a 20 ms PRI, the velocity of each body part could be approximately constant, where a maximum motion range is estimated within 200 mm, even in the case of a lower arm or leg. The WKD algorithm can also provide an instantaneous Doppler velocity at each PRI, and is applicable to time-variant motion. This is in contrast to STFT and other coherent integration methods in which the assumption of constant velocity over the integration period fundamentally limits temporal and velocity resolution. If we assume a realistic walking motion in which each body part is swung up, at some point the velocity of each part becomes zero, and this makes it difficult to unambiguously decompose range- τ points. Furthermore, with RPM imaging applied to each PRI, bi-directional processing (WKD \leftrightarrow RPM) is applicable to time-variant motion.

6 | EXPERIMENTAL VALIDATION

6.1 | Setup and parameters

The experimental tests, by using the X-band UWB radar system, have been demonstrated as follows. The experimental scene is shown in Figure 8. Here, the X-band UWB impulse radar by Sakura Tech Corp is introduced, where the centre frequency is 8.5 GHz and the 3-dB bandwidth is 1.5 GHz, indicating 100 mm theoretical range resolution. Broadband Fermi antennas, which have 40° 3-dB beamwidths for both E - and H -planes, are arranged on a plane of $y = 0$ mm, where four sets of transmitting and receiving Fermi antennas are horizontally arranged with 200 mm

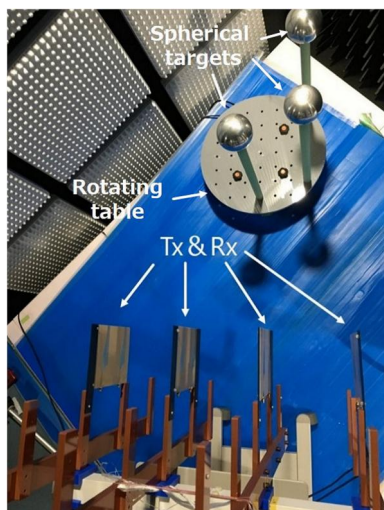


FIGURE 8 Experimental setup. Four sets of vertically aligned transmitter and receiver Fermi antennas are horizontally arranged. Three spherical metallic objects are rotated by the azimuth table

spacing separation, are horizontally arranged with 200 mm spacing. Here, monostatic observation is assumed, namely, the receiver only records the reflection signal from the transmitter at the same horizontal location, and then, each centre of the transmitter and receiver is defined as $(X_i, 0, Z_0)$, ($i = 1, \dots, 4$). Note that a strictly quantitative evaluation is hardly achieved in assuming a realistic human body with walking motion because true orbits of range and Doppler velocity profiles of such real humans could not be strictly determined, which would possibly lead to vague or inaccurate evaluations. Then, the three metallic spheres with 100 mm diameter are rotated along the vertical axis, to validate each method in the quantitative manner. The horizontal distance from the centre of the rotation table to the origin of the observation point is 475 mm, and that from each target to the rotation axis is 217 mm. The total number of pulse sequences is 37 with 152 ms PRI, denoting that the total observation time is 5.625 s. Stop and-go measurements for target rotation are carried out to acquire a quantitative profile for an actual range and Doppler velocity, where the rotation angle θ is varied for $0 \leq \theta \leq \pi$ with $\pi/36$ spacing.

6.2 | Results and discussions

First, we show the STFT-based Doppler velocity performance as in Figure 9, where its temporal window is set to 1.875 s, yielding a Doppler velocity resolution of 9 mm/s and an unambiguous Doppler velocity range of ± 0.058 m/s. Figure 9 demonstrates that the STFT suffers from considerably lower velocity resolutions compared to the theoretical one because its Doppler velocity considerably varies for the duration of the temporal range of the STFT. Furthermore, the dynamic range of the actual Doppler velocities is over 0.1 m/s, which is greater than the upper limit of the unambiguous velocity of 0.197 m/s. The above points are unavoidable limitations in the STFT-based approach.

6.2.1 | Case without data integration

Figure 10 shows the range- τ points profile, associated with the Doppler velocities obtained by each method at four antenna locations, and Figure 11 shows the Doppler velocity profile for the slow time at Antenna # 1, where the data integration scheme is not applied. These results show that the WKD method provides the Doppler velocities at each range- τ points, even when the Doppler velocity considerably varies along the slow-time direction, which is hardly obtained using the STFT or other coherence-based Doppler analysis as shown in Figure 9. This is the distinct advantage of the WKD method. Moreover, Figure 11b shows that the bi-directional data processing by RPM enhances the accuracy of the Doppler velocity estimations, especially for eliminating the unnecessary

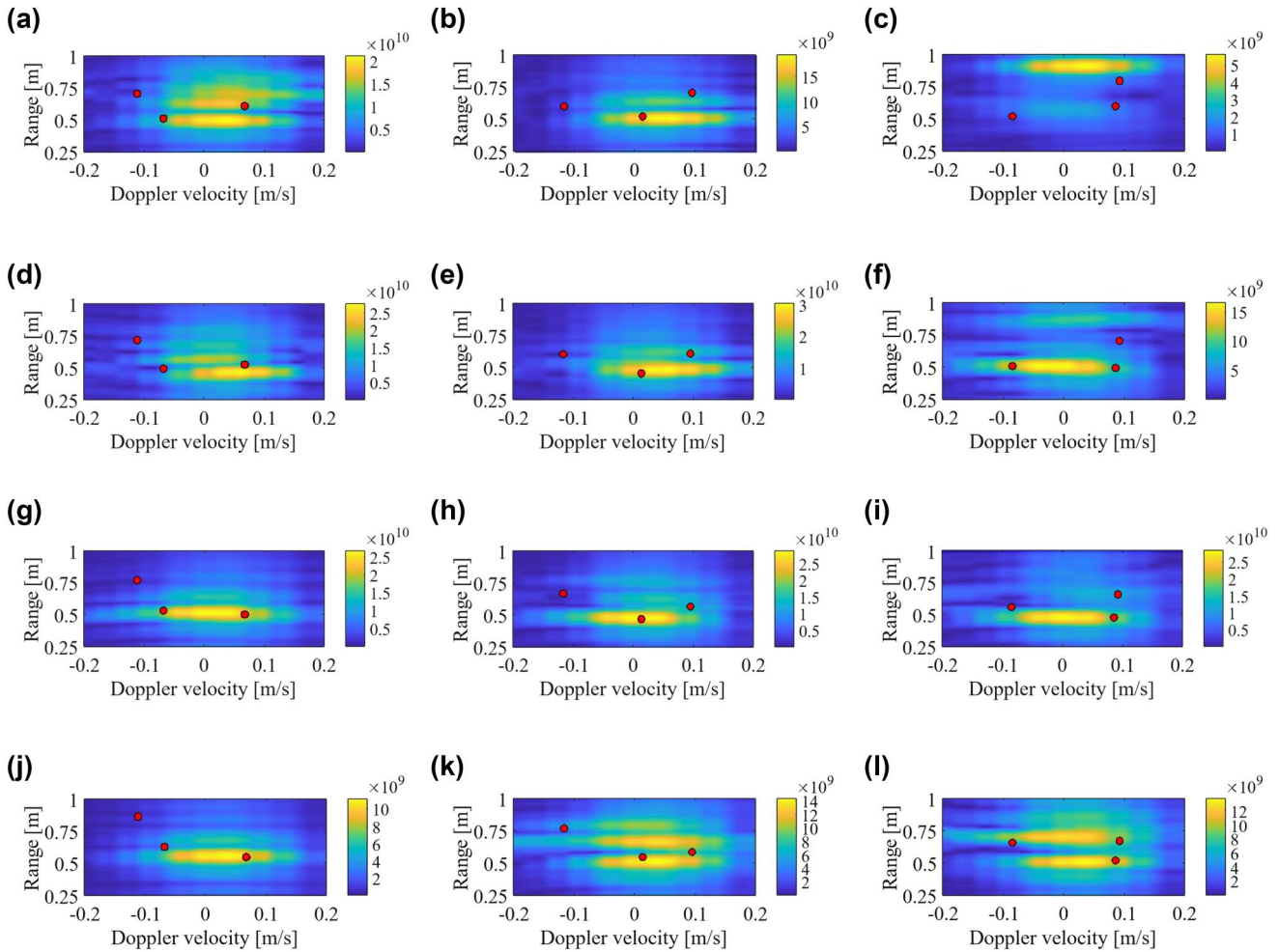


FIGURE 9 Range-Doppler velocity responses by the short-time Fourier transform (STFT)-based analysis with the temporal window width of 1.875 s. Red solid circles denote the actual Doppler velocity at the centre of each time window. The colour bar denotes the strength of the STFT responses. (a) $0 \text{ s} \leq \tau \leq 1.875 \text{ s}$, (b) $1.875 \text{ s} \leq \tau \leq 3.75 \text{ s}$, (c) $3.75 \text{ s} \leq \tau \leq 5.625 \text{ s}$, (d) $0 \text{ s} \leq \tau \leq 1.875 \text{ s}$, (e) $1.875 \text{ s} \leq \tau \leq 3.75 \text{ s}$, (f) $3.75 \text{ s} \leq \tau \leq 5.625 \text{ s}$, (g) $0 \text{ s} \leq \tau \leq 1.875 \text{ s}$, (h) $1.875 \text{ s} \leq \tau \leq 3.75 \text{ s}$, (i) $3.75 \text{ s} \leq \tau \leq 5.625 \text{ s}$, (j) $0 \text{ s} \leq \tau \leq 1.875 \text{ s}$, (k) $1.875 \text{ s} \leq \tau \leq 3.75 \text{ s}$, and (l) $3.75 \text{ s} \leq \tau \leq 5.625 \text{ s}$

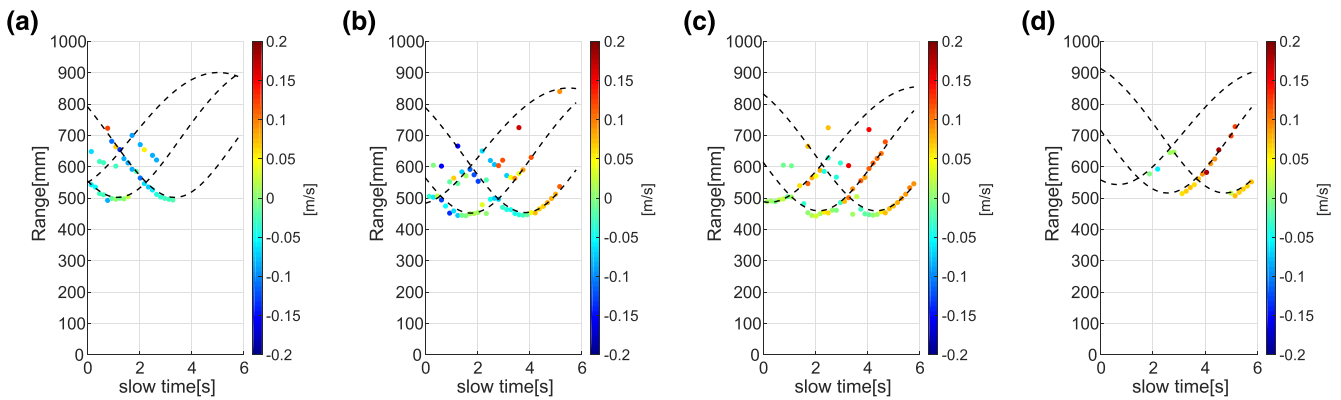


FIGURE 10 Range- τ points profile associated with the Doppler velocity by the proposed method at each antenna location. Colour denotes the Doppler velocities. (a) Antenna # 1, (b) Antenna # 2, (c) Antenna # 3, and (d) Antenna # 4

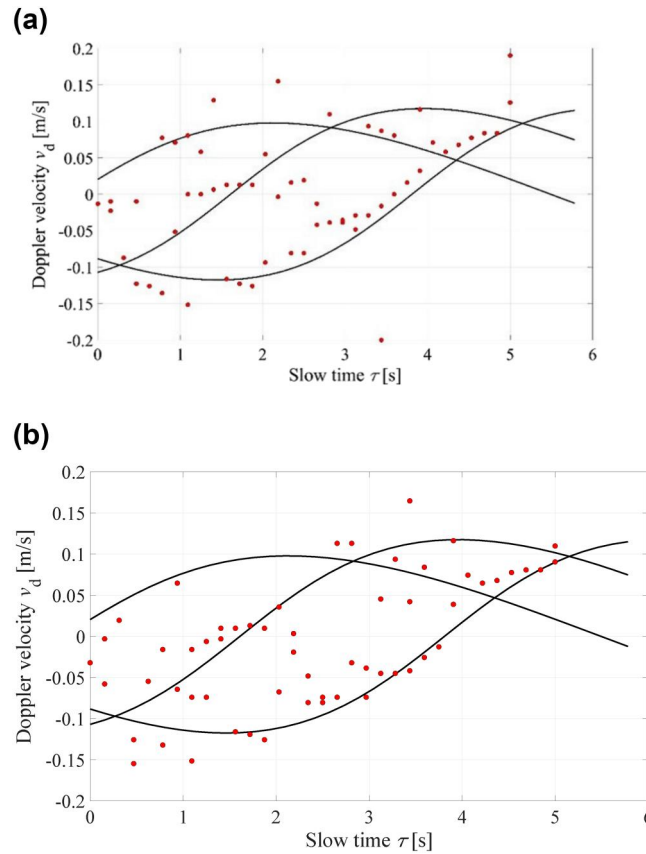


FIGURE 11 Doppler velocity estimations for each slow time τ , denoted by red dots. Three black curves show the true Doppler velocities of the three targets. (a) Method [31] and (b) proposed

estimations. Table 6 summarises the quantitative error analysis by calculating the cumulative probability in each criterion, in terms of the Doppler velocity and range. Here, note that the improvement using the proposed method is insignificant, compared with the results in the numerical simulation (Section 5). This is because the proposed method enhances the imaging of objects with multiple scattering points such as the human body. Because the experimental model deals with three separate spheres, a distinguished improvement is apparent. About RPM imaging performance, Figure 12 shows the reconstructed scattering centres obtained by the RPM method at each slow-time snapshot, where the range- τ points from the proposed method as shown in Figure 10 are processed. These results demonstrate that the number of reconstruction points by the RPM is too small to grasp the position of the target, and the part of them is far from the actual boundary because of the lack of data (four observation) being processed at each τ point. Also, the reflection signal from the back side position could not be clearly recorded by the shadow effect; thus the data integration scheme is required in this case. Furthermore, Table 5 compares the data processing time in each method, in which an Intel Xeon CPU E5-2637 v2 processor running at 3.5 GHz with 16 GB RAM is used. While the proposed method involves more computational complexity owing to the bi-directional

processing of the RPM, the total time taken is still within 1 s. This could be further reduced with a modification of the algorithm or processing code.

6.2.2 | Case with data integration

Finally, the data integration performance is investigated. Figures 13 and 14 show the Doppler velocity associated range- τ points profile and the Doppler velocity estimation along the slow time at Antenna # 1, respectively, where the neighbouring two range- τ points are integrated along the slow-time direction. As shown in Figure 13, we could confirm that the number of range- τ points significantly increased; it is expected that this data offers more informative and accurate Doppler or radar imaging. Table 6 shows the quantitative error test for data integration. While the cumulative probabilities for each error criteria are almost at the same level, the number of range- τ points with high accuracy increased. Finally, Figure 15 shows the RPM imaging results, where the integrated range- τ points are processed in Equation (6). While Figure 15 shows that some reconstruction points are deviated from the actual target boundary, many of them focussed on the vicinity of the target boundary. Table 7 summarises the quantitative error analysis and demonstrates the above point, that is, the

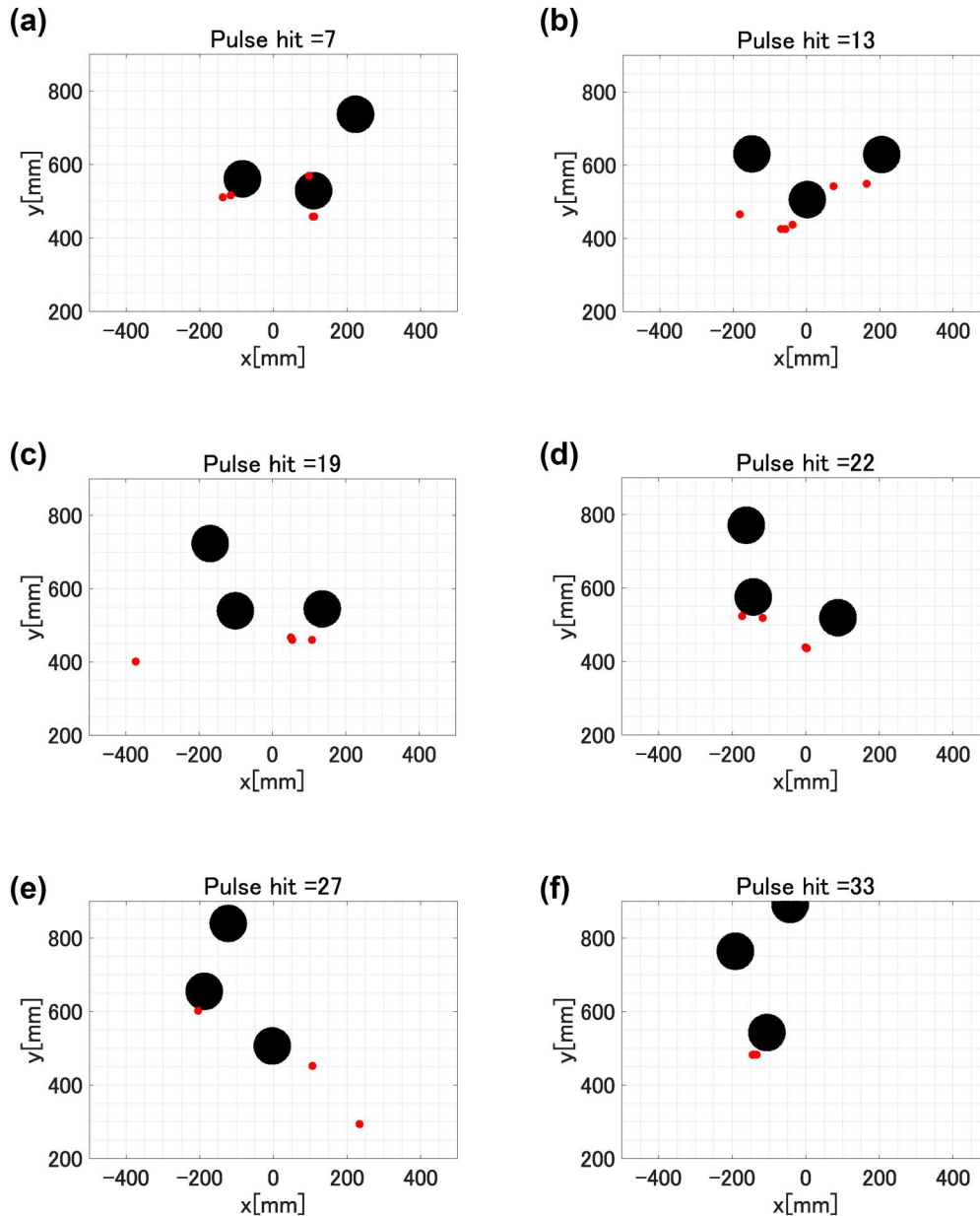


FIGURE 12 Results of target boundary reconstruction by the RPM at each slow time snapshot without slow-time data integration. (a) $\tau = \tau_7$, (b) $\tau = \tau_{13}$, (c) $\tau = \tau_{19}$, (d) $\tau = \tau_{22}$, (e) $\tau = \tau_{27}$, and (f) $\tau = \tau_{33}$

TABLE 5 Processing time required in each method

	Method [31]	Proposed method (WKD \rightarrow RPM \rightarrow WKD)
Processing time	0.1 s	0.9 s

Abbreviations: RPM, range points migration; WKD, weighted kernel density.

number of scattering centre points within a certain accuracy level is considerably enhanced, more than 3 times greater than those before integration, and achieved much less root mean square errors, compared with those that did not use data integration, which would provide a more reliable image to ensure the target position.

7 | CONCLUSION

To obtain more accurate Doppler and image profiles in the short-range sensing scenario, this study presents a novel radar data processing scheme associating Doppler velocity and radar imaging via WKD and RPM methods. The proposed method

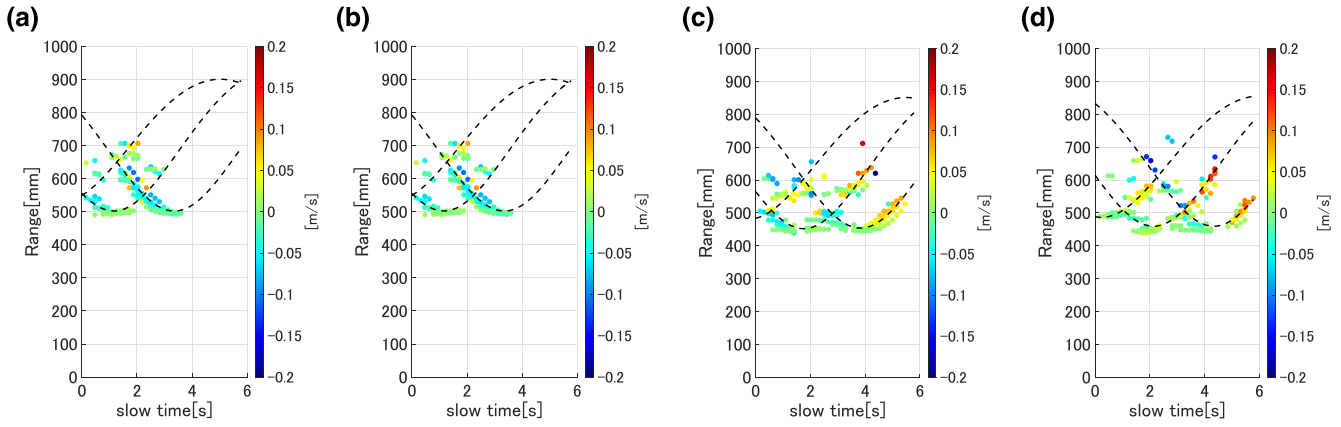


FIGURE 13 Range- τ points profile associated with the Doppler velocity by the proposed method at each antenna location with data integration along two neighbouring τ . Colour denotes the Doppler velocities. (a) Antenna # 1, (b) Antenna # 2, (c) Antenna # 3, and (d) Antenna # 4

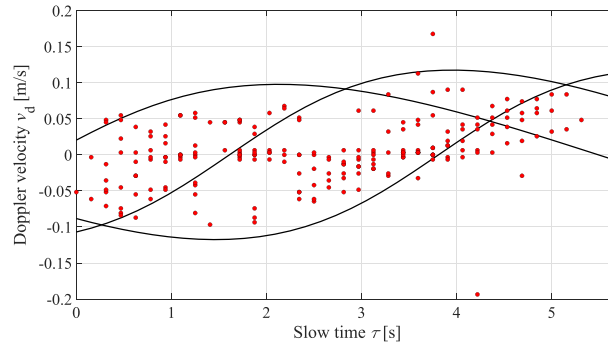


FIGURE 14 Doppler velocity estimations for each slow time τ , denoted by red dots, with data integration. Three black curves show the true Doppler velocities of the three targets. (a) Proposed

TABLE 6 Cumulative probability of each criteria in the Doppler velocity estimation in the experiment

	Method [31] w/o integ.	Proposed w/o integ.	Proposed w integ.
$ \Delta R \leq 30$ mm and $ \Delta v_d \leq 0.02$ m/s	10.2% (18/175)	9.7% (17/175)	8.4% (43/510)
$ \Delta R \leq 30$ mm and $ \Delta v_d \leq 0.05$ m/s	23.4% (41/175)	18.9% (33/175)	17.0% (87/510)

uses the unique features of the WKD estimator and RPM method, making the observable range- τ points reversibly associated with its Doppler velocity or scattering centre point on the target boundary. Processing from WKD to RPM allows us to eliminate unnecessary range- τ points during the optimisation process in the RPM method, which enhances the reconstruction accuracy. Processing from RPM to WKD, the WKD estimator, in terms of the scattering centre locations by the RPM method, upgrades the Doppler velocity estimation performance via appropriate data selection. This demonstrates that bi-directional data processing between Doppler velocity and imaging analysis can be enhanced for both the WKD estimator and the RPM method. Furthermore, range compensation schemes, by the obtained Doppler velocity at

each pulse hit, enable us to achieve accurate data integration along the slow-time profile direction before the RPM process, which could enhance both imaging accuracy and the number of imaging points. The 3-D FDTD numerical tests, using a simplified human body model, demonstrated that using the bi-directional data processing method remarkably enhances accuracy in both Doppler velocity and RPM imaging and demonstrated that this data integration scheme offers more accurate and informative radar images to help recognise the target shape. Moreover, the X-band UWB radar experiments using three metallic spheres also validate the effectiveness of the proposed method, in terms of the point that it increases the reconstruction points with higher accurate Doppler velocity and scattering centres. While this study presents only

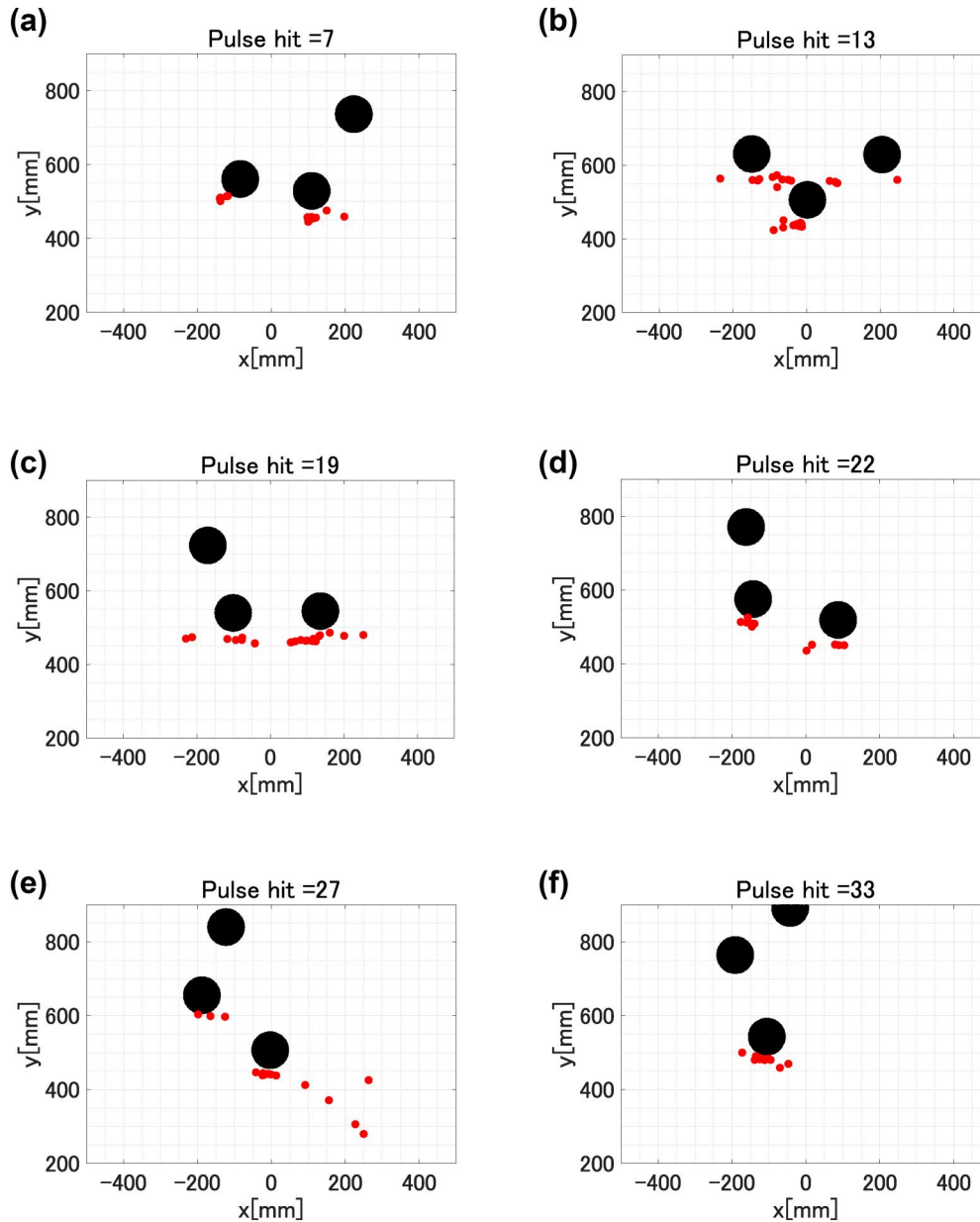


FIGURE 15 Results of target boundary reconstruction by the RPM at each slow time snapshot with slow-time data integration. (a) $\tau = \tau_7$, (b) $\tau = \tau_{13}$, (c) $\tau = \tau_{19}$, (d) $\tau = \tau_{22}$, (e) $\tau = \tau_{27}$, and (f) $\tau = \tau_{33}$

TABLE 7 Cumulative probability and RMSE for RPM imaging with or without data integration using the experimental data

	Cumulative probability		RMSE
	Err \leq 20 mm	Err \leq 50 mm	
Proposed w/o integ.	28.5% (49/172)	29.6% (178/601)	164.0 mm
Proposed w integ.	29.6% (178/601)	77.8% (468/601)	81.1 mm

Abbreviation: RMSE, root mean square errors.

metallic spheres in the experiment to validate the method in a quantitative manner, it would provide an advantage for the case in a realistic human walking scenario, by increasing more number of imaging or velocity estimations.

ACKNOWLEDGEMENT

This research is funded by Japan Science and Technology Agency, Precursory Research for Embryonic Science and Technology, grant number JPMJPR1771.

DATA AVAILABILITY STATEMENT

The data that support the findings of this study are available from the corresponding author upon reasonable request.

ORCID

Shoubei Kidera  <https://orcid.org/0000-0002-2993-5649>

REFERENCES

- Guo, S., et al.: Behind corner targets location using small aperture millimeter wave radar in NLOS urban environment. *IEEE J. Sel. Top. Appl. Earth. Obs. Remote. Sens.* 13, 460–470 (2020)
- Rabaste, O., et al.: Around-the-corner radar: detection of a human being in non-line of sight. *IET Radar, Sonar Navig.* 9(6), 660–668 (2015)
- Vinh, D., Ozlem, K.: Simulation framework for compressive sensing-based through-wall detection of moving targets. *IET Radar, Sonar Navig.* 11(9), 1349–1358 (2017)
- Lai, P.C., et al.: Hilbert–Huang transform analysis of human activities using through-wall noise and noise-like radar. *IET Radar, Sonar Navig.* 2(4), 244–255 (2008)
- Setsu, M., Kidera, S.: Range points migration and Doppler based multipath exploitation method for UWBThrough-the-wall radar. *IET Radar, Sonar Navig.* 13(1), 50–57 (2018)
- Li, H., et al.: Robust human targets tracking for MIMO through-wall radar via multi-algorithm fusion. *IEE J. Sel. Top. Appl. Earth. Obs. Remote. Sens.* 12(4), 1154–1164 (2019)
- Kim, Y., Ha, S., Kwon, J.: Human detection using Doppler radar based on physical characteristics of targets. *Geosci. Rem. Sens. Lett. IEEE.* 12(2), 289–293 (2015)
- Shi, X., et al.: Radar echoes simulation of human movements based on MOCAP data and EM calculation. *Geosci. Rem. Sens. Lett. IEEE.* 16(6), 859–863 (2019)
- Wagner, T., Feger, R., Stelzer, A.: Radar signal processing for jointly estimating tracks and micro-Doppler signatures. *IEEE Access.* 5, 1220–1238 (2017)
- Dave, T.: Review of micro-Doppler signatures. *IET Radar, Sonar Navig.* 9(9), 1140–1146 (2015)
- Svante, B., Henrik, P., Gustaf, H.: Features for micro-Doppler based activity classification. *IET Radar, Sonar Navig.* 9(9), 1181–1187 (2015)
- Shiqi, D., et al.: Radar-based human identification using deep neural network for long-term stability. *IET Radar, Sonar Navig.* 14(10), 1521–1527 (2020)
- Chen, V.C., et al.: Micro-Doppler effect in radar: phenomenon, model, and simulation study. *IEEE Trans. Aerosp. Electron. Syst.* 42(1), 2–21 (2006)
- Clemente, C., Soraghan, J.J.: Vibrating target micro-Doppler signature in bistatic SAR with a fixed receiver. *IEEE Trans. Geosci. Remote Sens.* 50(8), 3219–3227 (2012)
- Le Kernec, J., Li, C.: Continuous human motion recognition with a dynamic range-Doppler trajectory method based on FMCW radar. *IEEE Trans. Geosci. & Remote Sens.* 57(9), 6821–6831 (2019)
- Li, M., Chen, T., Du, H.: Human behavior recognition using range-velocity-time points. *IEEE Access.* 8, 37914–37925 (2020)
- Gustafsson, M., et al.: Extraction of human micro-Doppler signature in an urban environment using a “sensing-behind-the-corner” radar. *Geosci. Rem. Sens. Lett. IEEE.* 13(2), 187–191 (2016)
- Easton, R.L., Ticknor, A.J., Barrett, H.H.: Two-dimensional complex Fourier transform via the Radon transform. *Appl. Opt.* 24, 3817–3824 (1985)
- Xu, J., et al.: Radon-Fourier transform (RFT) for radar target detection (I): generalized Doppler filter bank processing. *IEEE Trans. Aero. Electron. Syst.* 47(2), 1186–1202 (2011)
- Chen, X.L., et al.: Maneuvering target detection via Radon-Fractional Fourier transform-based long-time coherent integration. *IEEE Trans. Signal Process.* 62(4), 939–953 (2014)
- Xu, J., et al.: Space-time Radon–Fourier transform and applications in radar target detection. *IET Radar, Sonar Navig.* 6(9), 846–857 (2012)
- Suresh, P., et al.: Extracting micro-Doppler radar signatures from rotating targets using Fourier-Bessel transform and time-frequency analysis. *IEEE Trans. Geosci. & Remote Sens.* 52(6), 3204–3210 (2013)
- Huang, P.H., et al.: Long-time coherent integration for weak maneuvering target detection and high-order motion parameter estimation based on keystone transform. *IEEE Trans Signal Process.* 64(15), 4013–4026 (2016)
- Sun, Z., et al.: Detection of weak maneuvering target based on keystone transform and matched filtering process. *Signal Process.* 140, 127–138 (2017)
- Zeng, T., et al.: Ground-based SAR wide view angle full-field imaging algorithm based on keystone formatting. *IEEE J. Sel. Top. Appl. Earth. Obs. Remote. Sens.* 9(6), 2160–2170 (2016)
- Carlson, B.D., Evans, E.D., Wilson, S.L.: Search radar detection and track with the Hough transform(I):System concept. *IEEE Trans. Aero. Electron. Syst.* 30(1), 102–108 (1994)
- Carlson, B.D., Evans, E.D., Wilson, S.L.: Search radar detection and track with the Hough transform(II):Detection statistics. *IEEE Trans. Aero. Electron. Syst.* 30(1), 109–115 (1994)
- Hosein, O.A., Ali, S.M.: Coherent method for ground-moving target indication and velocity estimation using Hough transform. *IET Radar, Sonar Navig.* 11(4), 646–655 (2017)
- Pang, C., Liu, S., Han, Y.: Coherent detection algorithm for radar maneuvering targets based on discrete polynomial-phase transform. *IEEE J. Sel. Top. Appl. Earth. Obs. Remote. Sens.* 9, 3412–3422 (2019)
- Noto, M., Shang, F., Kidera, S., Kirimoto, T.: Super-resolution time of arrival estimation using random resampling in compressed sensing. *IEICE Trans. Commun.* E101(6), 1513–1520 (2018)
- Setsu, M., et al.: Super-resolution Doppler velocity estimation by kernel based range- τ point conversions for UWB short range radars *IEEE Trans. Geosci. & Remote Sens.* 58(4), 2430–2443 (2020)
- Kidera, S., Sakamoto, T., Sato, T.: Accurate UWB radar three-dimensional imaging algorithm for a complex boundary without range point connections. *IEEE Trans. Geosci. Remote Sens.* 48(4), 1993 (2004)
- Gonzalez-Valdes, B., et al.: Improving security screening: a comparison of multistatic radar configurations for human body imaging. *IEEE Antenn. Propag. Mag.* 58(4), 35–47 (2016)
- Soldovieri, F., et al.: A Kirchhoff-based shape reconstruction algorithm for the multimonostatic configuration: the realistic case of buried pipes. *IEEE Trans. Geosci. Remote Sens.* 46(10), 3031–3038 (2008)
- Sun, H., et al.: High-resolution anisotropic prestack Kirchhoff dynamic focused beam migration. *IEEE Sensor J.* 20(20), 11753–11760 (2020)
- Lopez-Sanchez, J.M., Fortuny-Guasch, J.: 3-D radar imaging using range migration techniques. *IEEE Trans. Antennas & Propagat.* 48(5), 728–737 (2000)
- Wang, Z., et al.: Near-field 3-D millimeter-wave imaging using MIMO RMA with range compensation. *IEEE Tran. Microw. Theor. Tech.* 67(3), 1157–1166 (2019)
- Amineh, R.K., et al.: Three-dimensional near-field microwave holography using reflected and transmitted signals. *IEEE Trans. Antenn. Propag.* 59(12), 4777–4789 (2011)
- Gaikovich, K.P., et al.: Subsurface near-field microwave holography. *IEEE J. Sel. Top. Appl. Earth. Obs. Remote. Sens.* 9(1), 74–82 (2016)
- Tajik, D., et al.: Real-time microwave imaging of a compressed breast phantom with planar scanning. *IEEE J. Electromagn. RF Microw. Med. Biol.* 2(3), 154–162 (2018)
- Sasaki, Y., et al.: Three-dimensional imaging method incorporating range points migration and Doppler velocity estimation for UWB

- millimeter-wave radar. *IEEE Geosci. Remote Sens. Letts.* 14, 122–126 (2017)
42. Hayashi, T., Kidera, S.: Bi-directional processing algorithm with RPM and WKD based Doppler velocity estimator for 3-D Doppler-radar imaging. *Proc. 2020 IEEE Geoscience and Remote Sensing Symposium* (2020)
 43. Akiyama, Y., Kidera, S.: Low complexity algorithm for range-point migration-based human body imaging for multistatic UWB radars. *IEEE Geosci. & Remote Sens. Lett.* 16(2), 216–220 (2019)

How to cite this article: Hayashi, T., Ando, T., Kidera, S.: Three-dimensional Doppler-associated radar imaging method based on bi-directional data processing. *IET Radar Sonar Navig.* 16(1), 145–160 (2022). <https://doi.org/10.1049/rsn2.12171>